PROCEEDINGS A

royalsocietypublishing.org/journal/rspa

Research

Cite this article: Rolf-Pissarczyk M, Wollner MP, Pacheco DRQ, Holzapfel GA. 2021 Efficient computational modelling of smooth muscle orientation and function in the aorta. *Proc. R. Soc. A* **477**: 20210592.
https://doi.org/10.1098/rspa.2021.0592

Received: 21 July 2021
Accepted: 18 October 2021

Subject Areas:
biomedical engineering, biomechanics

Keywords:
constitutive modelling, fibre dispersion, smooth muscle cell, contraction, discrete fibre dispersion model

Author for correspondence:
Gerhard A. Holzapfel
e-mail: holzapfel@tugraz.at

Electronic supplementary material is available online at https://doi.org/10.6084/m9.figshare.c.5705324.

THE ROYAL SOCIETY
PUBLISHING

Efficient computational modelling of smooth muscle orientation and function in the aorta

Malte Rolf-Pissarczyk[1], Maximilian P. Wollner[1,3], Douglas R. Q. Pacheco[2] and Gerhard A. Holzapfel[1,4]

[1]Institute of Biomechanics, and [2]Institute of Applied Mathematics, Graz University of Technology, Graz, Austria
[3]Institute for Solid Mechanics, Dresden University of Technology, Dresden, Germany
[4]Department of Structural Engineering, Norwegian University of Science and Technology (NTNU), Trondheim, Norway

GAH, 0000-0001-8119-5775

Understanding the mechanical effects of smooth muscle cell (SMC) contraction on the initiation and the propagation of cardiovascular diseases such as aortic dissection is critical. Framed by elastic lamellar sheets in the lamellar unit, there are SMCs in the media with a distinct radial tilt, which indicates their contribution to the radial strength. However, the mechanical effects of this type of anisotropy have not been fully discussed. Therefore, in this study, we propose a constitutive framework that models the passive and active mechanics of the aorta, taking into account the dispersed nature of the aortic constituents by applying the discrete fibre dispersion method. We suggest an isoparametric approach by evaluating various numerical integration methods and introducing a non-uniform discretization of the unit hemisphere to increase its computational efficiency. Finally, the constitutive parameters are fitted to layer-specific experimental data and initial computational results are briefly presented. The radial tilt of SMCs is also analysed, which has a noticeable influence on the mechanical behaviour of the aorta. In the absence of sufficient experimental data, the results indicate that the active contribution of SMCs has a remarkable impact on the mechanics of the healthy aorta.

© 2021 The Author(s) Published by the Royal Society. All rights reserved.

Downloaded from https://royalsocietypublishing.org/ on 17 November 2021

Downloaded from https://royalsocietypublishing.org/ on 17 November 2021

1. Introduction

The aorta is a complex living organ that plays a crucial role in the cardiovascular system. Its functioning can only be understood as a physiological interplay between the passive and active constituents of the aorta, which is disturbed in cardiovascular disease. In aortic aneurysms and dissections, Shen & LeMaire [1], for example, showed that the connection between smooth muscle cells (SMCs) and elastic fibres is disrupted, which could alter the role of SMCs as mechanosensors.

The aortic wall consists of three layers: intima, media and adventitia, in which several constituents are interwoven with each other to form a complex matrix. The media consists of about 53–78 stacked so-called lamellar units [2]. Each lamellar unit is framed by elastic lamellar sheets on the top and bottom, which are connected to one another by elastic fibres. Collagen fibres with relatively circumferential orientation and SMCs, which have either a contractile or a synthetic function, are embedded in the ground substance between the lamellar sheets. The active behaviour of the aortic wall is defined exclusively by contractile SMCs, more precisely by the microscopic movement of myosin–actin filaments in the contractile units of SMCs (e.g. [3]). The contractile units that define the direction of contraction are predominantly aligned parallel to the longitudinal axis of the SMCs [4,5]. Normally, only the cell nuclei are visible in structural examinations, which in turn are aligned with the longitudinal axis of the SMCs [6]. Several experimental studies have shown that the orientation of the SMCs has an alternating radial tilt of approximately $\pm 20^\circ$ [2,7,8], i.e. the cells are not completely aligned with the axial–circumferential plane. The resulting pattern is called the herringbone pattern [9], which is shown in figure 1*a*. However, the influence of this pattern on the radial strength in the healthy and also in the diseased aortic wall is not well understood. Interestingly, the value of the radial tilt is close to the angle of the first principal direction in the radial–circumferential plane, which led to the suggestion that SMCs extend in the direction of greatest strain [11]. The phenotype of SMCs is essential for vascular homeostasis, so an imbalance between the contractile phenotype, which changes the luminal diameter, and the synthetic or proliferative phenotype, which responds to environmental biochemical stimuli, is known as a marker for cardiovascular disease. More specifically, Humphrey [12] hypothesized that apoptosis and dysfunction of SMCs are associated with aortic dissection, among other factors. To support this hypothesis, Halushka *et al.* [10] compared normal aortic tissue of a young adult with pathological medial tissue, as shown in figure 1*b*,*c* with different magnifications. In pathological medial tissue, they found that SMC nuclei can be lost in a patchy and band-like fashion, as shown in figure 1*d*,*e*, respectively. The SMC nuclei are shown in dark blue/burgundy colouring. These researchers referred to the band-like loss of SMCs as 'laminar medial collapse', which corresponds to the historical nomenclature of 'laminar medial necrosis' or 'laminar necrosis' (see, for example, the studies on dissected tissue [13,14]). Other experimental evidence was published by Lee *et al.* [15] in an immunohistochemical study on dissected medial tissues. It is thus obvious that apoptosis and dysfunction of SMCs make an important contribution to the initiation and propagation of an aortic dissection but also to the development of other cardiovascular diseases.

The aim of this study is threefold: first, we present a constitutive framework based on the discrete fibre dispersion (DFD) method [16] that models the passive and active mechanics of the aorta; second, we propose an isoparametric DFD method and implement a non-uniform discretization of the unit hemisphere in order to increase computational efficiency; finally, the structural and mechanical parameters of the aortic constituents are validated with experimental data from our laboratory and from the literature using a maximum-likelihood estimation (MLE) and a least-squares (LSQ) regression and the initial computational results of a healthy aorta are shown. Whenever possible, we use experimental data from a dissected human aorta for future applications to computational studies of aortic dissections. However, the lack of sufficient experimental data prevents the aim from presenting a constitutive model of the passive and active mechanics of the dissected human aorta. Instead, datasets from various human donors and animals are used, some from healthy and some from dissected tissues. In particular, there is a lack of experimental data on the active contribution of SMCs in healthy and diseased human aortas.

Downloaded from https://royalsocietypublishing.org/ on 17 November 2021

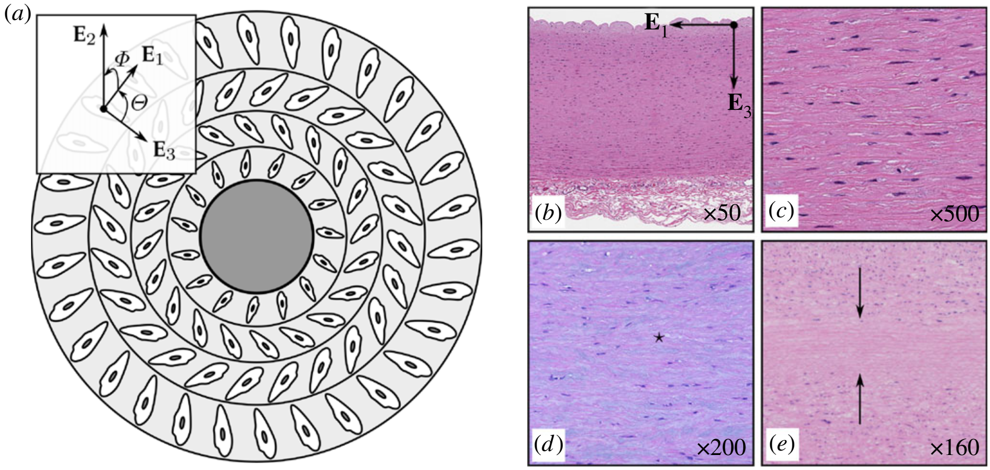

Figure 1. (*a*) Schematic two-dimensional representation of the SMC arrangement (herringbone pattern) with $\mathbf{E}_1$, $\mathbf{E}_2$ and $\mathbf{E}_3$ for the Cartesian unit basis vectors. Modified from Rhodin [9]. (*b*) Low and (*c*) high magnification of normal aortic tissue of a young adult showing all three aortic layers: intima (top), media and adventitia. SMC nuclei loss in (*d*) a patchy (asterisk) and (*e*) a band-like fashion (arrows) in pathological medial tissue. The SMC nuclei are shown in dark blue/burgundy. Histological images reprinted from Halushka *et al.* [10]. (Online version in colour.)

Therefore, experimental length–tension results of healthy animal tissue were scaled to human tissue.

The layer-specific constitutive model of the aorta includes the passive contribution of collagen fibres, elastic fibres and the ground substance, and, in addition, the active contribution of SMCs. This model is intended to provide a constitutive framework for the development of future large-scale computational studies to investigate healthy and diseased aortas. Against this background, the mechanochemical processes that trigger the active contraction of SMCs are eliminated in favour of a quasi-static and purely mechanical model that approximates the experimental data of aortic tissue in a contracted equilibrium. We therefore present a novel strain-energy function for modelling the active contribution of SMCs, which attempts to take into account the characteristic length–tension behaviour of SMCs and their dispersed transmural arrangement. First, we include the fraction of contractile SMCs and the maximum induced active SMC stiffness using two scalar factors. Second, we apply the framework of the DFD method to account for the dispersed arrangement of the contractile SMCs. Owing to the limited experimental data available, we model the dispersion of SMCs instead of the dispersion of the contractile units [3]. Third, the state of deformation of the SMCs prior to contraction is taken into account. Finally, the overlap behaviour of the contractile units of SMCs is described by a distribution function to include the efficiency with which it operates.

Section 2 proposes a layer-specific constitutive model that includes the passive and active mechanics of the aorta using the original DFD method [16]. Then, in §3, different numerical integration methods are compared and a non-uniform discretization of the unit hemisphere is assessed by plotting the convergence rates for representative numerical examples. In addition, an isoparametric DFD method is proposed and applied to a large-scale computational model from an earlier study to examine computational time and numerical results for several levels of discretization. The constitutive model for each constituent is then validated with experimental data in §4. Histological parameters are determined by an MLE with statistical data that define the arrangement of the respective constituents. The remaining mechanical material constants are then fitted to the results of uniaxial extension tests from our laboratory using LSQ regressions. Finally, the results are summarized in §5 and future prospects are discussed.

Downloaded from https://royalsocietypublishing.org/ on 17 November 2021

2. Layer-specific model framework

This section presents the continuum mechanical framework of a layer-specific constitutive model of the aorta. In addition to the passive material behaviour, the framework incorporates a mechanical model, which describes the active contribution of SMCs and also residual stresses. As outlined by Holzapfel *et al.* [17], there are several ways to model the dispersion of fibrous constituents, including the DFD method. In the following, the original DFD method, as it was introduced by Li *et al.* [16], is applied by discretizing the unit hemisphere into a finite number of elementary areas in order to model the dispersed alignment of collagen and elastic fibres, but also the dispersed transmural arrangement of SMCs in the aortic wall.

(a) Original discrete fibre dispersion method

In order to apply the DFD method, we define a probability density function (PDF) $\rho(\Theta, \Phi)$, which gives the probability of a fibrous constituent oriented along the unit vector

$$\mathbf{N}(\Theta, \Phi) = \sin\Theta\cos\Phi\,\mathbf{E}_1 + \sin\Theta\sin\Phi\,\mathbf{E}_2 + \cos\Theta\,\mathbf{E}_3, \tag{2.1}$$

where $\mathbf{E}_i$, $i = 1, 2, 3$, define the Cartesian unit basis vectors. Thus, the unit vector $\mathbf{N}(\Theta, \Phi)$ lies on the unit hemisphere $\mathbb{S} = \{(\Theta, \Phi) | \Theta \in [0, \pi], \Phi \in [0, \pi]\}$. For reasons of symmetry, we only need to consider half of the unit hemisphere. The DFD method requires the discretization of the unit hemisphere into a finite number of elementary areas $\Delta\mathbb{S}_n$, $n = 1, \ldots, m$, e.g. spherical triangles or angular elements, as depicted in §3b.

Next, a representative fibre direction $\mathbf{N}_n$ is defined in the centre of each elementary area $\Delta\mathbb{S}_n$ with the representative fibre angle (Θ_n, Φ_n). The discrete fibre density ρ_n is then calculated by numerical integration of the continuous fibre PDF over the corresponding elementary area, i.e.

$$\rho_n = \frac{1}{2\pi} \int_{\Delta\mathbb{S}_n} \rho(\Theta, \Phi) \sin\Theta\, \mathrm{d}\Theta\, \mathrm{d}\Phi, \quad n = 1, \ldots, m. \tag{2.2}$$

Note that the computational efficiency and accuracy depend strongly on the discretization and the numerical integration method used, which will be discussed later. A general strain-energy function Ψ per unit reference volume is then formulated in the discrete setting as

$$\Psi = \sum_{n=1}^{m} \rho_n \Psi_n(I_{4n}), \tag{2.3}$$

where $I_{4n} = \mathbf{C} : \mathbf{N}_n \otimes \mathbf{N}_n$ is the squared fibre stretch in the representative fibre direction $\mathbf{N}_n$ and $\Psi_n(I_{4n})$ is the single fibre strain energy. The right Cauchy–Green tensor $\mathbf{C} = \mathbf{F}^T\mathbf{F}$ is defined by the deformation gradient $\mathbf{F}$, which describes the deformation of a body from the reference to some current configuration [18]. The choice of (2.3) must ensure that the condition $\psi(1) = \psi'(1) = 0$ holds. Naturally, the discrete fibre density must fulfil the normalization condition in the discrete setting

$$\sum_{n=1}^{m} \rho_n = 1, \tag{2.4}$$

up to a numerical integration error.

(b) Passive constitutive model

The ground substance is described by the isotropic neo-Hookean model, specified by the strain energy Ψ_g, which depends on the first invariant $I_1 = \mathbf{C} : \mathbf{I}$, i.e.

$$\Psi_g(I_1) = \frac{\mu_g}{2}(I_1 - 3), \tag{2.5}$$

where μ_g represents the stiffness parameter and **I** is the second-order unit tensor. Based on the anisotropic nature of collagen fibres, elastic fibres and SMCs, these are modelled using the DFD method.

We assume that the total strain-energy function of the dispersed collagen fibres Ψ_c is given by

$$\Psi_c = \sum_{n=1}^{m} \rho_{cn} \Psi_{cn}(I_{4n}). \tag{2.6}$$

In order to exclude compressed collagen fibres within a dispersion, we then introduce the tension–compression switch

$$\Psi_{cn}(I_{4n}) = \begin{cases} f_c(I_{4n}) & \text{if } I_{4n} \geq 1, \\ 0 & \text{if } I_{4n} < 1, \end{cases} \tag{2.7}$$

and apply the strain-energy function of a two-dimensional (2D) single collagen fibre proposed by Holzapfel *et al.* [19], namely

$$f_c(I_{4n}) = \frac{k_1}{2k_2}\{\exp[k_2(I_{4n}-1)^2]-1\}, \tag{2.8}$$

where the collagen fibre stiffness and shape parameters are given by $k_1 > 0$ and $k_2 > 0$, respectively. In general, the DFD method is capable of any type of fibre dispersion, symmetric or non-symmetric, but Holzapfel *et al.* [20] have suggested a bivariate von Mises distribution. This distribution involves the introduction of a multiplicative split of the continuous PDF into an out-of-plane and an in-plane fibre dispersion as

$$\rho_c(\Theta, \Phi) = \rho_{c,\text{op}}(\Theta)\rho_{c,\text{ip}}(\Phi) \tag{2.9}$$

with

$$\rho_{c,\text{op}}(\Theta) = 2\sqrt{\frac{2b_c}{\pi}}\frac{\exp(-2b_c\cos^2\Theta)}{\text{erf}\,(\sqrt{2b_c})} \quad \text{and} \quad \rho_{c,\text{ip}}(\Phi) = \frac{\exp(a_c\cos 2\Phi)}{I_0(a_c)}, \tag{2.10}$$

where $I_0(x)$ and $\text{erf}(x)$ denote the modified Bessel function of the first kind of order zero and the error function of (x), respectively. The parameters $a_c > 0$ and $b_c > 0$ determine the concentration of fibres around the mean fibre orientation, i.e. $\Theta = \pi/2$ and $\Phi = 0$ in the local coordinate system of the fibre family. For the transformation into global coordinates (see figure 1), the collection of representative fibre directions $\mathbf{N}_n$ associated with ρ_{cn} must be rotated by some out-of-plane mean fibre angle $\Theta_{0,c}$ and in-plane mean fibre angle $\Phi_{0,c}$. The discrete fibre densities of (2.9) are then obtained by using (2.2). The choice of (2.10) naturally fulfils the normalization condition in the discrete setting (see (2.4)), and of course the normalization condition is also satisfied in the continuous setting, i.e.

$$\int_0^\pi \rho_{c,\text{op}}(\Theta)\sin\Theta\,\mathrm{d}\Theta = 2 \quad \text{and} \quad \frac{1}{\pi}\int_0^\pi \rho_{c,\text{ip}}(\Phi)\,\mathrm{d}\Phi = 1. \tag{2.11}$$

Note that the integrals of the normalization conditions can be solved in closed form, as explicitly shown in the electronic supplementary material, part B, in order to compute the out-of-plane and in-plane PDFs, i.e. (2.10).

Based on Rolf-Pissarczyk *et al.* [21] we now define the constitutive model for elastic fibres, specified by the strain energy Ψ_e, i.e.

$$\Psi_e = \sum_{n=1}^{m} \rho_{en} \Psi_{en}(I_{4n}), \tag{2.12}$$

and exclude fibres under compression as

$$\Psi_{en}(I_{4n}) = \begin{cases} f_e(I_{4n}) & \text{if } I_{4n} \geq 1, \\ 0 & \text{if } I_{4n} < 0. \end{cases} \tag{2.13}$$

In order to exclude degraded elastic fibres, (2.13) can easily be extended by introducing a degradation parameter, as introduced in [21]. Next, we define the mathematical expression of

Downloaded from https://royalsocietypublishing.org/ on 17 November 2021

Downloaded from https://royalsocietypublishing.org/ on 17 November 2021

the strain-energy function per 2D single fibre as

$$f_e(I_{4n}) = \frac{c_1}{c_2}(I_{4n}^{c_2/2} - 1) - c_1 \ln I_{4n}^{1/2}, \tag{2.14}$$

where c_1 and c_2 are the elastic fibre stiffness and the shape parameters, respectively, restricting (2.14) to the tension domain with $c_1 > 0$ and $c_2 \geq 2$ [22]. Note that (2.14) is motivated by recent experiments on a single elastic lamella [23]. In analogy with (2.10), the dispersion of elastic fibres is also described by a non-symmetric von Mises distribution.

The existence of a residual stress field $\widetilde{\mathbf{S}}$ adds another tensor-valued variable to the strain-energy function of a tissue. According to Ogden [24], the influence of residual stresses on the aorta is in the form

$$\Psi_{\text{res}} = \frac{1}{2}(\widetilde{\mathbf{S}} : \mathbf{C} - \widetilde{\mathbf{S}} : \mathbf{I}) \quad \text{with} \quad \boldsymbol{\sigma}_{\text{res}} = \frac{1}{J}\mathbf{F}\widetilde{\mathbf{S}}\mathbf{F}^T. \tag{2.15}$$

If the generally inhomogeneous residual stresses are to be taken into account, i.e. $\widetilde{\mathbf{S}}(\mathbf{x}) \neq \mathbf{0}$, the stress contribution $\boldsymbol{\sigma}_{\text{res}}$ must be added to the total Cauchy stress of the aorta.

Finally, we define the passive behaviour of the medial and adventitial layers by providing the strain-energy functions in each case according to

$$\Psi_{\text{med}} = -p(J-1) + \Psi_g + \sum_{i=1}^{2} \Psi_{ci} + \Psi_e + \Psi_{\text{res}} \tag{2.16}$$

and

$$\Psi_{\text{adv}} = -p(J-1) + \Psi_g + \sum_{i=1}^{2} \Psi_{ci} + \Psi_{\text{res}}, \tag{2.17}$$

where p denotes the Lagrange multiplier that is to be enforced by the incompressibility constraint $J = \det \mathbf{F} \equiv 1$. In addition, we assume the existence of two collagen fibre families i for each layer.

(c) Active contribution of SMCs

The active contraction of SMCs is triggered by a biochemical stimulus and involves molecular kinetics, which can enable the description of the temporal evolution of contractile SMCs [25]. Based on this, a series of papers was produced on this description [3,26–28], while the thermodynamics of mechanochemical coupling was dealt with in [29,30]. At this point, we neglect the mechanochemical processes that trigger the contraction of SMCs in favour of a quasi-static and purely mechanical model that approximates the characteristic length–tension behaviour of SMCs [31], because the time scale of interest is considerably longer than the activation duration of contraction. To also include dynamic *in vivo* loading conditions, one could use the configurational framework according to [28]. The deformation gradient is then described by a multiplicative decomposition into an elastic elongation of the attached cross-bridges and a part related to the relative sliding between the actin and myosin filaments. We consider this approach to be exaggerated for the present study.

We model the SMCs as being dispersed in the aortic wall, which implicitly also reflects the dispersion of the contractile units. This modelling approach is explained with experimental data: (i) the contractile units of SMCs are distributed with respect to the cellular axis [32] and (ii) the nuclei of SMCs are distributed around the mean orientation [33]. A common set-up for a length–tension experiment is the uniaxial extension test with an applied stretch λ in the direction of the expected mean orientation of the SMC arrangement, which is usually in the $\mathbf{E}_1$-direction. First, the passive nominal stress P^{pas} is recorded in order to obtain the passive behaviour of the aorta together with chemically suppressed contractile SMCs. Then with a fixed stretch λ, the contraction of SMCs is triggered, which provides the overall response of the aorta P^{tot}. In the literature, the active contribution of SMCs is calculated as $P^{\text{act}} = P^{\text{tot}} - P^{\text{pas}}$, although the transverse deformation before and after the contraction is different. Length–tension experiments as well as studies with a similar set-up were carried out on different mammalian species, e.g. with

Downloaded from https://royalsocietypublishing.org/ on 17 November 2021

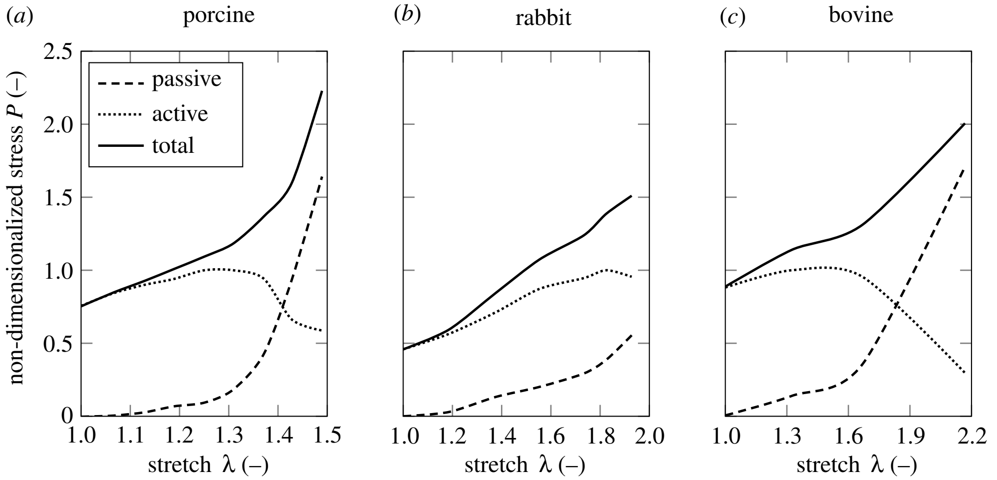

Figure 2. The passive, total and active stress responses from length–tension experiments with healthy (*a*) porcine tissue [35], (*b*) bovine tissue [34] and (*c*) rabbit tissue [41]. Note that the legend in (*a*) also applies to (*b*,*c*).

healthy bovine [34], porcine [26,35,36], canine [37–40], rabbit [41] and rat tissue [42]. However, the literature documents only a few experimental examples on human tissue [43,44] and none on human vascular tissue.

As shown in figure 2 for porcine, rabbit and bovine tissues, the length–tension experiments on different mammalian species show similarities. This finding by de Beaufort *et al.* [45] suggests that results from other mammals can also be transferred to human tissue. Note that the nominal stresses are non-dimensionalized by dividing with $\max P^{\text{act}}$. The stress–stretch curves show a general trend independent from the species. The passive material behaviour shows the expected exponential stiffening of the tissue. By contrast, the active behaviour demonstrates stress even without applied stretch, which illustrates its inelastic nature, and an asymmetrical drop on both sides of the maximum at which the contractile units operate most efficiently [44,46]. In addition, it can also be seen that the magnitude of the active behaviour depends on the deformation state $\mathbf{F}_0$, which is the state that the SMCs are in during the initial activation.

Two approaches were proposed to implement the results of the length–tension experiments in a quasi-static, continuum mechanical framework. Both approaches treat the active contribution of SMCs as an additional stress on top of the passive behaviour and assume that the overlap efficiency depends exclusively on the current deformation state $\mathbf{F}$ instead of $\mathbf{F}_0$. A first approach approximates the overlap behaviour by a parabola [47–49]. By contrast, a second approach uses a Gaussian function with two parameters to describe the overlap behaviour [36,50–52], which has the advantage that the contraction decays to zero far away from the efficiency maximum of the contractile unit instead of dropping below zero, which is non-physical. Interestingly, Haspinger *et al.* [53] have shown that the standard Gaussian function is generally not suitable for describing the asymmetry of the active behaviour.

Finally, within the setting of the original DFD method, we propose a new constitutive model of contractile SMCs, say Ψ_{smc}, as

$$\Psi_{\text{smc}} = \sum_{n=1}^{m} \rho_{\text{smc}n} \Psi_{\text{smc}n}(I_{4n}), \tag{2.18}$$

with the explicit mathematical expression of discrete SMCs

$$\Psi_{\text{smc}n}(I_{4n}) = \phi_{\text{smc}} \frac{\mu_{\text{smc}}}{2} \mathcal{O}(I_{0n})(I_{4n} - 1), \tag{2.19}$$

Downloaded from https://royalsocietypublishing.org/ on 17 November 2021

where $\mu_{\text{smc}} > 0$ represents the maximum induced active SMC stiffness and $0 \leq \phi_{\text{smc}} \leq 1$ represents the fraction of contractile SMCs. As already mentioned, the efficiency of the contractile units of SMCs depends on the initial deformation state $\mathbf{C}_0 = \mathbf{F}_0^T\mathbf{F}_0$, which can either be prescribed or taken from a previous simulation. The initial deformation state refers to the invariant $I_{0n} = \mathbf{C}_0 : \mathbf{N}_n \otimes \mathbf{N}_n$. This invariant can be understood as the deformation state of a discrete SMC pre-contraction. Based on experimental evidence, the efficiency of the contractile units of SMCs resembles a Weibull distribution of the form

$$\mathcal{O}(I_{0n}) = \left(\frac{I_{0n}}{I_{\text{opt}}}\right)^{\beta-1} \exp\left\{-\frac{\beta-1}{\beta}\left[\left(\frac{I_{0n}}{I_{\text{opt}}}\right)^{\beta} - 1\right]\right\}, \tag{2.20}$$

which has a maximum at $I_{\text{opt}} > 0$, with $\mathcal{O}(I_{\text{opt}}) = 1$, and by choosing the shape parameter $\beta > 0$ the function drops asymmetrically to zero.

Since the media consists of several lamellar units with an inhomogeneous arrangement of SMCs, the different radial tilt induces a transmural inhomogeneity in the media when the contraction of SMCs is triggered. Therefore, the active contribution of SMCs for each lamellar unit needs to be added to the passive behaviour of the media. Remodelling can be another factor that leads to additional transmural inhomogeneity [54], whereby each of the parameters in (2.19) and (2.20) may be a function of the reference position $\mathbf{X}$. Given the lack of sensitive experimental data, ϕ_{smc}, μ_{smc}, I_0 and β are assumed to be constant across the media.

3. Isoparametric discrete fibre dispersion method

In the following, we propose an isoparametric DFD method based on an updated numerical integration scheme and introduce a non-uniform discretization of the unit hemisphere to increase computational efficiency.

(a) Numerical integration of the discrete fibre density

First, we compare the numerical integration method of the original DFD method with Gaussian quadrature rules of different orders in order to assess the quality of the result. In the original DFD method, the integral of (2.2) is calculated with high accuracy by dividing each elementary area into about a thousand smaller areas and applying the vertex rule to each of them [55].

Even if not explicitly stated, the underlying mathematical assumption in (2.3) is that the strain-energy function $\Psi_n(I_{4n})$ is approximately constant in every elementary area, i.e. only the variation of $\rho(\Theta, \Phi)$ within each $\Delta\mathbb{S}_n$ is taken into account. While this might make sense under certain conditions, the isoparametric approach would be to use the value of $\rho(\Theta, \Phi)$ at the centroid instead of evaluating the integral of (2.2) to a very high precision. To distinguish between the two approaches, we use the notation ρ_n from (2.3) for the discrete (integrated) fibre density used by the DFD method and ϱ_n for the discrete fibre density at the centroid, i.e. $\varrho_n = \rho(\mathbf{N}_n)$. The isoparametric approach would then correspond to the well-known centroid integration rule [56], which for our case reads

$$\Psi = \frac{1}{2\pi}\sum_{n=1}^{m} |\Delta\mathbb{S}_n| \varrho_n \Psi_n(I_{4n}), \tag{3.1}$$

where $|\Delta\mathbb{S}_n|$ denotes the surface area of $\Delta\mathbb{S}_n$. This approach has the same order of convergence as the previous one, i.e. the integration error tends to zero in both cases at the same asymptotic rate as $m \to \infty$. The reason for this is that, regardless of how high the integration order for the computation of ϱ_n is, the low-order error that is introduced by fixing $\Psi_n(I_{4n})$ at the centroid dominates. It is known that the centroid rule often performs even better than some higher order integration rules [56], especially in the presence of discontinuities that occur when excluding fibres under compression. In addition, the centroid scheme is extremely simple to implement as it does not require isoparametric transformations for quadrature rules. Fortunately, there are analytical expressions to find both the centroid position and the area of spherical elements. In

Downloaded from https://royalsocietypublishing.org/ on 17 November 2021

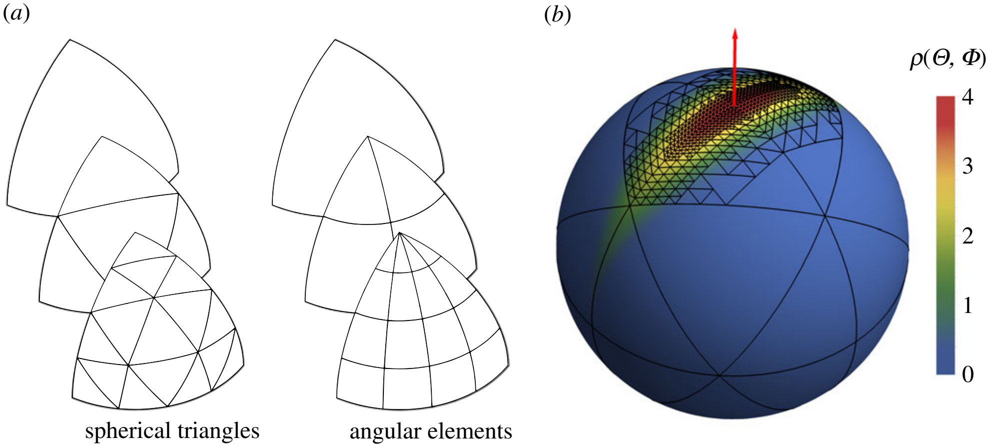

Figure 3. (*a*) Uniform discretization of a unit hemisphere segment using spherical triangles and angular elements; (*b*) illustrative non-uniform discretization of a unit hemisphere with $m = 1024$ spherical triangles, applied to a non-symmetric PDF of collagen fibres, represented by a bivariate von Mises distribution with the mean fibre direction (red arrow) and the concentration parameters $b_a = 1$ and $a_c = 13$, which are introduced in (2.9). (Online version in colour.)

other words, if the unit hemisphere is discretized, all the ingredients necessary to carry out the integration are readily available.

(b) Non-uniform discretization of the unit hemisphere

Li *et al.* [16] suggested that a local refinement of areas on the unit hemisphere to account for locally concentrated fibre dispersion could be beneficial. This could be of particular interest for modelling non-symmetric fibre dispersions. Based on this idea, we present now a method in the following to locally refine areas on the unit hemisphere.

As shown in figure 3*a*, we consider two types of elementary areas: spherical triangles, which are treated in Cartesian coordinates, and angular elements, which are formed by the tensor product of the angular coordinates Θ and Φ. Each of these has advantages and disadvantages. When meshing, the angular elements are a bit simpler, since a mesh can be formed by simply crossing a Θ-grid with a Φ-grid. Triangular elements can, however, be refined indefinitely without loss of shape [57], while successive uniform refinements of angular elements lead to a progressive slimming of the elementary areas close to the pole, as shown in figure 3*a*.

Let $\mathbf{v}_1$, $\mathbf{v}_2$ and $\mathbf{v}_3$ be the position vectors for the vertices of a spherical triangle $\Delta\mathbb{S}$. The position of the centroid is simply

$$\mathbf{N} = \frac{\mathbf{v}_1 + \mathbf{v}_2 + \mathbf{v}_3}{|\mathbf{v}_1 + \mathbf{v}_2 + \mathbf{v}_3|}, \tag{3.2}$$

and the surface area is given by l'Huilier's theorem [58]

$$|\Delta\mathbb{S}| = 4 \arctan\left[\sqrt{\tan\left(\frac{t}{2}\right)\tan\left(\frac{t-u}{2}\right)\tan\left(\frac{t-v}{2}\right)\tan\left(\frac{t-w}{2}\right)}\right], \tag{3.3}$$

in which $u = \arccos(\mathbf{v}_3 \cdot \mathbf{v}_2)$, $v = \arccos(\mathbf{v}_3 \cdot \mathbf{v}_1)$, $w = \arccos(\mathbf{v}_1 \cdot \mathbf{v}_2)$ and $2t = u + v + w$.

By contrast, the area of an angular element $\Delta\mathbb{S} = (\Theta_1, \Theta_2) \times (\Phi_1, \Phi_2)$ is given explicitly by

$$|\Delta\mathbb{S}| = |(\Theta_2 - \Theta_1)(\cos\Phi_1 - \cos\Phi_2)|, \tag{3.4}$$

and its centroid coordinates (Θ^*, Φ^*) are such that $2\Theta^* = \Theta_1 + \Theta_2$ and $2\cos\Phi^* = \cos\Phi_1 + \cos\Phi_2$. The application of the centroid rule is therefore straightforward for both types of elementary area. On the other hand, if a different integration rule is used, it is generally necessary to first map

Downloaded from https://royalsocietypublishing.org/ on 17 November 2021

between the curved and a flat reference elementary area and then to apply standard Gaussian integration rules defined on such a reference elementary area. For further details, the reader is referred to the literature [56,59]. It is noteworthy that the mapping of angular elements is somewhat easier to handle, since higher order integration rules can be constructed by simply combining one-dimensional quadrature formulae in both directions.

Since the fibre density varies considerably with respect to the direction, uniformly discretizing the unit hemisphere may not be a very efficient approach. A truly adaptive refinement requires knowing the integrand beforehand, which is unfortunately not the case here. In this case, the integrand of (3.1) depends on the deformation gradient, which of course is not known *a priori*. The only information we have *a priori* is the PDF of the fibres $\rho(\Theta, \Phi)$. We therefore propose an alternative local refinement criterion based on a coarse, uniform mesh. A certain elementary area $\Delta\mathbb{S}_n$ is refined if the condition $\varrho_n > \varrho_{\max}$ holds, where $\varrho_{\max}$ represents a predefined maximum value. This refinement is applied consecutively until the criterion is met for all elementary areas, which guarantees that more refinement is carried out in regions with a higher fibre concentration. An illustrative non-uniform discretization of the unit hemisphere with spherical triangles is shown in figure 3*b*.

(c) Evaluation of convergence rates

Then we implemented various numerical integration methods and the non-uniform discretization of the unit hemisphere for spherical triangles and angular elements in Matlab [60]. We decided to compare the Gaussian quadrature rule of order 1 (GQR1) and 4 (GQR4) with the numerical integration method used by the original DFD method. The numerical integration method of the DFD method can of course only be used for spherical triangles. To assess the quality of the results, we first systematically solved two representative numerical examples, uniaxial extension and simple shear of a unit cube, with the finite-element analysis program FEAP [61]. The numerical results of this finite-element analysis are validated with the analytical solution from Matlab [60] and Mathematica [62]. For a detailed description of the two representative examples, the reader is referred to Li *et al.* [16]. Second, we applied the large-scale computational model of a patient data-motivated geometry of an aortic dissection introduced by Rolf-Pissarczyk *et al.* [21], which has been implemented in the commercially available finite-element analysis program Abaqus/Standard [63], in order to compare the computational time and the computational results obtained with several discretization levels. Here we limited the evaluations to representative results.

Figure 4*a*,*b* compares the convergence rates obtained from a uniaxial extension test. Note that the discrete nature of the DFD method does not allow a continuous evaluation. We have connected the evaluation points with solid lines for illustration.

The use of a non-uniform discretization only allows additional evaluation points. The results of the uniform and non-uniform discretizations show that the various numerical integration methods provide comparable convergence rates for spherical triangles and angular elements. Interestingly, the results of the numerical integration method used in the original DFD method and the GQR4 are almost identical. When comparing the performance of the two elementary area types, the discretization with spherical triangles provides higher convergence rates for all numerical integration methods. In addition, the non-uniform discretization shows a better convergence rate with a smaller number of elementary areas. For example, the accuracy of the non-uniform discretization falls below a specified relative error of 10^{-2} with significantly fewer elementary areas than the uniform discretization for GQR1. However, with a higher number of elementary areas, the results always seem to converge, which implies that we only benefit from a non-uniform refinement when using a small number of elementary areas. In addition, the non-uniform discretization of angular elements shows no improvement over the uniform discretization. It is noteworthy that the results were independent of the finite-element mesh.

The simple shear test gave similar results, as shown in figure 5, but with some striking differences. First, the convergence rate achieved with the GQR1 for both types of elementary

Downloaded from https://royalsocietypublishing.org/ on 17 November 2021

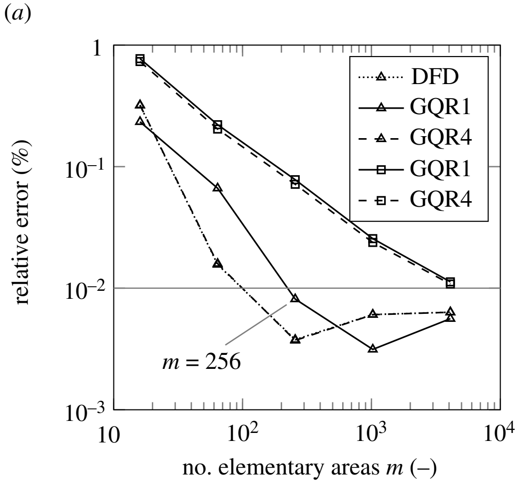

Figure 4. Convergence rates obtained from a uniaxial extension test with symmetric fibre distribution and a concentration parameter $b = 2.0$ [16]. The graph shows the comparison of (i) the numerical integration method used by the DFD method, GQR1 and GQR4, (ii) the (*a*) uniform and (*b*) non-uniform discretization of the unit hemisphere and (iii) the discretization of the unit hemisphere with spherical triangles and angular elements.

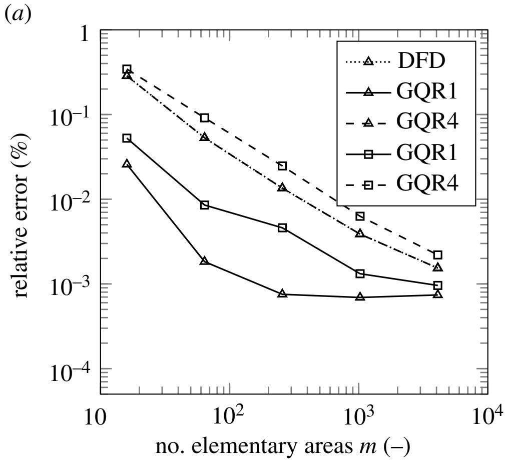

Figure 5. Convergence rates obtained from a simple shear test with symmetric fibre distribution and a concentration parameter $b = 2.0$ [16]. The graph shows the comparison of (i) the numerical integration method used by the DFD method, GQR1 and GQR4, (ii) the (*a*) uniform and (*b*) non-uniform discretization of the unit hemisphere and (iii) the discretization of the unit hemisphere with spherical triangles and angular elements.

area is significantly higher than the other numerical integration methods that evaluate the PDF in each elementary area with several integration points. Second, the convergence rates of the uniform discretization are comparable to or even better than those of the non-uniform discretization. Therefore, the non-uniform discretization shows no advantages for this particular boundary-value problem.

After analysing the discretization with representative examples, the isoparametric DFD method is applied to the computational model of a patient data-motivated geometry of an aortic dissection introduced by Rolf-Pissarczyk *et al.* [21], as shown in figure 6*a*. For details about the created geometry, the applied boundary conditions at systole, the chosen spatial and time discretizations of the geometry and the numerical solver used, including the specifications of the computer, the reader is referred to [21]. Since the exclusion of collagen and elastic fibres

Downloaded from https://royalsocietypublishing.org/ on 17 November 2021

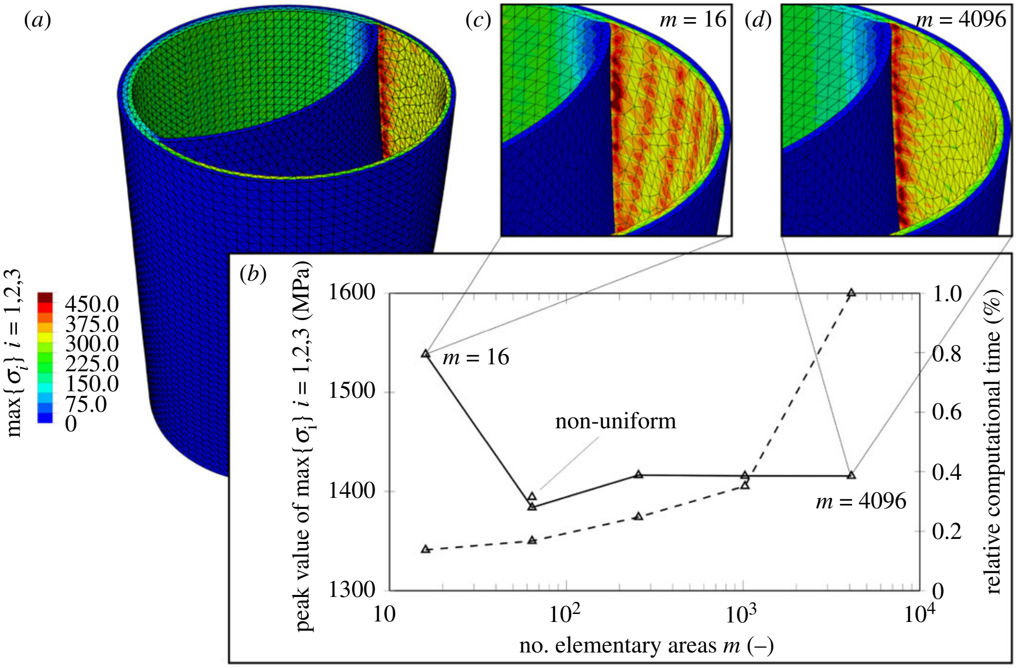

Figure 6. Application of the computational model introduced by Rolf-Pissarczyk *et al.* [21] of a patient data-motivated geometry of an aortic dissection to compare the influence of the number of elementary areas (spherical triangles) (i) on the computational time and (ii) on the computational results: (*a*) maximum principal stress $\max\{\sigma_i\}_{i=1,2,3}$ obtained with 4096 elementary areas and a uniform discretization; (*b*) comparison of the peak value of $\max\{\sigma_i\}_{i=1,2,3}$ (solid line) and the relative computational time (dashed line) when using several discretization levels; (*c*,*d*) $\max\{\sigma_i\}_{i=1,2,3}$ for $m = 16$ and $m = 4096$, respectively. (Online version in colour.)

influences the comparison of the computational time, but also the numerical convergence of this particular boundary-value problem, we have neglected the exclusion of fibres owing to both fibre compression and degradation. With respect to numerical convergence, we identified that a low number of elementary areas leads to problems when excluding a significant number of areas. This finding is plausible, since, for example, if we exclude a single elementary area of the unit hemisphere, the relative impact on the constitutive model is higher when discretizing with 16 areas than when discretizing with 4096 areas. In this particular boundary-value problem, we observed these problems for approximately 100 elementary areas and fewer areas.

Figure 6*a* illustrates the computational results, represented by the maximum principal stress $\max\{\sigma_i\}_{i=1,2,3}$, obtained with 4096 elementary areas and a uniform discretization of the unit hemisphere. Then, in figure 6*b*, the relative computational time and the peak value of $\max\{\sigma_i\}_{i=1,2,3}$ for several discretization levels with a uniform discretization are shown. By comparing the results obtained with 64 elementary areas for both uniform and non-uniform discretization, the advantage of a non-uniform discretization becomes apparent. In order to examine the influence of the number of elementary areas on the computational time but also on the computational results, figure 6*c*,*d* illustrates the $\max\{\sigma_i\}_{i=1,2,3}$ for 16 and 4096, respectively.

4. Model fitting

The determination of the constitutive parameters is described in detail in the following section. First, the structural parameters of the anisotropic constituents are derived from the histology. The remaining mechanical parameters are then fitted to experimental results and finally all the constitutive parameters obtained are summarized in tables.

Downloaded from https://royalsocietypublishing.org/ on 17 November 2021

Because of the scarcity of studies on human aortic tissue, it is not possible to use the results of a single experimental study to capture all material constants. For this reason, various constitutive parameters are fitted to different sets of experimental data that do not necessarily originate from the aorta, let alone from human tissue. Nevertheless, great attention is paid to the selection of the sources and their preparation, so that the applicability can be ensured. Note that we are neglecting transmural material inhomogeneities in the media and adventitia.

(a) Regression of structural parameters

The anisotropy of each aortic constituent, i.e. collagen fibres, elastic fibres and SMCs, is defined by a set of structural parameters. These parameters are now identified histologically using MLE.

(i) Collagen fibres

Histological data are usually provided in the form of histograms for an out-of-plane angle $\Theta_{c,\mathrm{op}}$ and an in-plane angle $\Phi_{c,\mathrm{ip}}$. The histological study of Schriefl *et al.* [64] suggests the existence of two separate fibre families in the $(\mathbf{E}_1, \mathbf{E}_2)$-plane with their respective in-plane mean fibre angles for healthy human thoracic aortic tissue. We also leave open the possibility of two different out-of-plane fibre families with the mean fibre angles. In order to reduce the model complexity, we assume that the concentration parameters a_c and b_c are the same for the respective fibre families in every layer and that the respective mean fibre directions are symmetric, i.e. $\pm\Theta_{0,c}$ and $\pm\Phi_{0,c}$.

The MLE is now used to determine, exemplarily, the set of structural parameters of the out-of-plane PDF $\{b_c, \Theta_{0,c}\}$, from the experimental data Θ_{cr}. Therefore, we define the out-of-plane PDF for two fibre families with regard to the normalization condition, shown in (2.11), as a superposition of two shifted von Mises distributions, i.e.

$$\rho_{c,\mathrm{op}}(\Theta) = \sqrt{\frac{2b_c}{\pi}}\,\frac{\exp[-2b_c\cos^2(\Theta-\Theta_{0,c})] + \exp[-2b_c\cos^2(\Theta+\Theta_{0,c})]}{\exp(-b_c)g(b_c,\Theta_{0,c})}, \tag{4.1}$$

where the explicit expression for $g(b_c, \Theta_{0,c})$ is given in the electronic supplementary material, part A. The MLE aims to optimize an objective function $\mathcal{L}_{c,\mathrm{op}}$ of some kind similar to other fitting algorithms, which is defined by the theoretical model at s experimentally measured data points. For the out-of-plane case, the objective function $\mathcal{L}_{c,\mathrm{op}}$ is in the form

$$\mathcal{L}_{c,\mathrm{op}}(b_c,\Theta_{0,c}) = \prod_{r=1}^{s}\rho_{c,\mathrm{op}}(\Theta_{cr}), \tag{4.2}$$

i.e. the product of all s probability density values at each data point Θ_{cr}. For this reason, the objective function $\mathcal{L}_{c,\mathrm{op}}$ is called the likelihood function in the context of MLE. If the assumed PDF actually represents the experimental observations, its set of parameters $\{b_c, \Theta_{0,c}\}$ must maximize the likelihood function, i.e.

$$\{b_c^*, \Theta_0^*\} = \underset{b_c\in[0,\infty),\Theta_{0,c}\in[0,(\pi/2)]}{\arg\max}\ \mathcal{L}_{c,\mathrm{op}}(b_c,\Theta_{0,c}). \tag{4.3}$$

For computational reasons it is often convenient to use the logarithm of the likelihood function, i.e. the log-likelihood function $l_{c,\mathrm{op}} = \ln\mathcal{L}_{c,\mathrm{op}}$, which by definition is maximized by the same set of parameters as $\mathcal{L}_{c,\mathrm{op}}$, since the logarithm is a strictly increasing function. At this maximum, the gradient of the log-likelihood function l_{op} must vanish, if the global maximum is not at the boundary of the parameter space. Therefore, we write

$$\left.\frac{\partial l_{c,\mathrm{op}}}{\partial b_c}\right|_{b_c^*,\Theta_{0,c}^*} = 0 \quad \text{and} \quad \left.\frac{\partial l_{c,\mathrm{op}}}{\partial \Theta_{0,c}}\right|_{b_c^*,\Theta_{0,c}^*} = 0, \tag{4.4}$$

which represents a nonlinear system of equations. The analytical expression of the derivatives in (4.4) is contained in the electronic supplementary material, part A. Since the solution of the above nonlinear system of equations cannot be expressed in closed form, numerical methods are used to

Downloaded from https://royalsocietypublishing.org/ on 17 November 2021

Table 1. Summary of the regression results of the structural and mechanical parameters for both the media and the adventitia, which are based on experimental results from the literature; [23]—healthy porcine thoracic aorta; [64]—healthy human thoracic aorta; [33]—healthy human aorta.

		value			R^2 (%)	
constituent	parameter	media	adventitia	reference	media	adventitia
ground substance	μ_g	6.18 kPa	6.18 kPa	[–][a]	99.95	99.62
collagen fibres	k_1	10.75 kPa	27.86 kPa	[–][a]	99.95	99.62
	k_2	1.38	1.38	[23]	97.08	97.08
	a_c	3.62	3.08	[64]		
	b_c	34.30	33.20	[64]		
	$\Phi_{0,c}$	±25.14°	±50.72°	[64]		
	$\Theta_{0,c}$	90.0°	90.0°	[64]		
elastic fibres	c_1	62.97 kPa		[–][a]	99.95	
	c_2	2.98		[23]	99.74	
	b_e	34.30		[–][b]		
	$\Theta_{0,e}$	90.0°		[–][b]		
SMCs	a_{smc}	4.07		[33]		
	$\Phi_{0,\text{smc}}$	0.0°		[33]		
	b_{smc}	$+\infty$		[–][b]		

[a] Laboratory of the Institute of Biomechanics—dissected human ascending thoracic aorta.

[b] Assumption.

calculate b_c^* and $\Theta_{0,c}^*$, e.g. the built-in function *fsolve* from the Python library *SciPy*. The necessary starting values for the algorithm are selected by visualizing the log-likelihood function $l_{c,\text{op}}$ in a contour plot and identifying the approximate location of the global maximum.

Analogously to this, the set of structural parameters $\{a_c, \Phi_{0,c}\}$ of the assumed in-plane PDF in (2.10) is determined from the experimental data Φ_{cr} through the maximization problem. For the in-plane data, it is assumed that at most two fibre families are visible in the in-plane histogram, so that the in-plane PDF takes the form

$$\rho_{c,\text{ip}}(\Phi) = \frac{\exp\{a_c \cos[2(\Phi - \Phi_{0,c})]\} + \exp\{a_c \cos[2(\Phi + \Phi_{0,c})]\}}{2I_0(a_c)}. \tag{4.5}$$

The results of the regression are shown in table 1. The logarithm of the likelihood function of the in-plane PDF, i.e. the log-likelihood function $l_{c,\text{ip}}$, and the analytical expressions of its derivatives are contained in the electronic supplementary material, part A. Four structural parameters $\{a_c, b_c, \Phi_{0,c}, \Theta_{0,c}\}$ were determined for each layer. In addition, a comparison between the histological data and the regression results for the media and adventitia are given in the electronic supplementary material, part C. Here, the maximum number of two out-of-plane and in-plane fibre families is sufficient to approximate the histological data.

(ii) Elastic fibres and SMCs

Experimental studies on the arrangement of human elastic fibres that could be used to perform an MLE similar to the collagen fibres are rare. In fact, we were unable to trace any suitable experimental data. Therefore, the PDF of elastic fibres and their statistical parameters are chosen so that they approximate the qualitative observations. Since elastic fibres are usually arranged in a sheet-like structure, the so-called elastic lamellae, it is assumed that they are mainly oriented in the $(\mathbf{E}_1, \mathbf{E}_2)$-plane with a certain distribution in the radial direction. Interestingly, it turned out that

Downloaded from https://royalsocietypublishing.org/ on 17 November 2021

Table 2. Summary of the regression results of the mechanical parameters of contractile SMCs for different radial tilts, which are based on scaled experimental results from the literature [26]; [26]—healthy porcine common carotid artery.

radial tilt (°)	μ_{smc} (kPa)	I_{opt} (—)	β (—)	R^2 (%)
0	149.31	1.39	2.84	77.30
10	152.27	1.38	2.90	77.29
20	162.43	1.34	3.09	77.27
30	184.09	1.29	3.40	77.23
40	226.58	1.22	3.83	77.17
50	316.35	1.13	4.32	77.13

elastic fibres show a slight difference between the $\mathbf{E}_1$-direction and the $\mathbf{E}_2$-direction [65]. Based on this and analogous to (2.10), the concentration parameter of the elastic fibres b_e is equal to the out-of-plane concentration parameter of the collagen fibres b_c. The in-plane concentration parameter a_e is set to zero. The structural parameters of elastic fibres are listed in table 1.

Only one experimental study was found to investigate the distribution of SMCs in healthy human thoracic aortic tissue [33], albeit exclusively in-plane. In addition, similar studies used porcine tissue [52,66]. Because of the frequently reported helical arrangement of SMCs, it is assumed that the in-plane PDF has the same form as collagen fibres, but with a different set of structural parameters $\{a_{\text{smc}}, \Phi_{0,\text{smc}}\}$. It is remarkable that the global maximum for the MLE is determined at the in-plane angle $\Phi_{0,\text{smc}} = 0^\circ$, i.e. the two assumed families of SMCs are indistinguishable. This is in contrast to the original paper, which identified the angle $\Phi_{0,\text{smc}} = 8.4^\circ$ [33].

Experimental data for the out-of-plane distribution are even more sparse. Although the herringbone pattern of SMCs is reported qualitatively in several publications, a statistical analysis of the radial tilt, which resolves each lamellar unit separately, was only carried out for murine tissue [7,8] to the knowledge of the authors. Theoretically, each lamellar unit can have an individual radial tilt, so that the number of possible configurations increases rapidly. For the sake of simplicity, it is assumed that the magnitude of the radial tilt remains constant over all elastic lamellar units and, in addition, a set of six different tilts $\{0^\circ, 10^\circ, 20^\circ, 30^\circ, 40^\circ, 50^\circ\}$ is chosen *a priori* to investigate the mechanical impact. Owing to the lack of reliable experimental data, the out-of-plane concentration parameter is assumed to be $b_{\text{smc}} \to \infty$. The results of the regression of the six different sets of mechanical parameters $\{\mu^*_{\text{smc}}, I^*_{\text{opt}}, \beta^*\}$ for the six radial tilts are listed in table 2.

(b) Regression of mechanical parameters

Next, the set of mechanical parameters of the passive constitutive model $\{\mu_g, k_1, k_2, c_1, c_2\}$ and the active contribution of SMCs $\{\mu_{\text{smc}}, I_{\text{opt}}, \beta\}$ are fitted to experimental data using an LSQ regression.

(i) Passive material response

The constitutive models of collagen and elastic fibres represent the material behaviour of a statistically representative fibre. In this context, it makes sense to determine their shape parameters k_2 and c_2 from the experimental data of a single collagen or elastic fibre. Here, we have chosen an elastic lamella instead of an elastic fibre, as we did not have any experimental data on the latter. In the experimental study by Matsumoto *et al.* [23], uniaxial extension tests were performed on a single adventitial collagen fibre and a medial elastic lamella, but both from a healthy porcine thoracic aorta. To obtain the set of mechanical parameters for collagen fibres

Downloaded from https://royalsocietypublishing.org/ on 17 November 2021

$\{k_1, k_2\}$, an error norm $\mathcal{S}$ was defined as

$$\mathcal{S}(k_1, k_2) = \sum_{r=1}^{s} [\mathcal{F}(\lambda_r, k_1, k_2) - \sigma_r]^2, \tag{4.6}$$

where $\mathcal{F}$ represents the constitutive model of the collagen fibres (see (2.6)), in connection with the boundary-value problem posed by a uniaxial extension test, which is the s stress–stretch pairs $\{\sigma_r, \lambda_r\}$. Then, the predicted stress response for a given stretch depends on the parameter set $\{k_1, k_2\}$, i.e. $\sigma = \mathcal{F}(\lambda_r, k_1, k_2)$. The aim is now to determine the specific parameter set $\{k_1^*, k_2^*\}$, i.e.

$$\{k_1^*, k_2^*\} = \underset{k_1\in[0,\infty), k_2\in[0,\infty)}{\arg\min} \quad \mathcal{S}(k_1, k_2). \tag{4.7}$$

This nonlinear optimization problem is then handled numerically by the *least-squares* built-in function from the Python library *SciPy*. However, it does not follow from this that the function $\mathcal{F}(\lambda_r, k_1^*, k_2^*)$ is actually a good approximation of the experimental data just because a global minimum is found. Therefore, a statistical measure is used to quantify the goodness of the fit. Here the usual coefficient of determination R^2 is chosen, i.e.

$$R^2 = 1 - \frac{\mathcal{S}(k_1^*, k_2^*)}{s\mathrm{Var}(\sigma_r)}, \tag{4.8}$$

where $\mathrm{Var}(\sigma_r)$ denotes the variance in the data σ_r.

The set of mechanical parameters for the elastic lamellae $\{c_1^*, c_2^*\}$ is determined in the same way. In addition, we assume that the shape parameter of the collagen fibres in the adventitia is also applicable to the media. For the fitting procedure of the adventitia and the media, the stiffness parameters $\{k_1^*, c_1^*\}$ are discarded, since the information about the stiffness of a single fibre cannot be easily transferred to the entire layer.

Next, the remaining set of mechanical parameters for the adventitia $\{\mu_g, k_1\}$ is determined. To do this, we used experimental data from our laboratory obtained from a dissected human ascending thoracic aorta. The experimental protocol of the uniaxial extension test follows the description of Weisbecker *et al.* [67]. The results of the uniaxial tests on the adventitia provided data points for the axial stretch and Cauchy stress component. We assume that the deformation is homogeneous and that the radial and circumferential surfaces of the specimen remain traction-free, so that the results of the LSQ regression provided the set of mechanical parameters for the adventitia $\{\mu_g^*, k_1^*\}$.

Then the set of mechanical parameters of the medial layer $\{k_1, c_1\}$ must be determined. Note that we have assumed that the stiffness of the ground substance μ_g^* is the same in both layers. Otherwise the LSQ regression would lead to the undesirable limit case $c_1^* = 0\,\mathrm{kPa}$. Our laboratory also provided unpublished experimental data points for the media of a dissected human ascending thoracic aorta $\{\lambda_{1r}, \sigma_{11r}\}$. Therefore, we apply the LSQ regression with the same assumptions as for the adventitia to determine the remaining set of mechanical parameters of the media $\{k_1^*, c_1^*\}$.

A comparison between the experimental data and the prediction of the constitutive model is shown in figure 7. We did not use the entire range of data points for the LSQ regression, for both layers $\lambda_{1,\max} = 1.45$ and $\lambda_{2,\max} = 1.30$, because the exponential increase in stiffness for larger stretches in the non-physiological stretch regime would have led to non-physical material behaviour. In addition, there is a trade-off between the regression quality of each parameter and the sensibility of the simulation results. More precisely, an exact fit to these experimental data of the adventitia could also be possible for the non-physiological regime, but the adventitia would show an unphysically stiff behaviour in the simulations. Determining the mechanical parameters is a compromise and it is expected that the constitutive models for the various constituents will reflect the experimental data qualitatively rather than quantitatively. The results of the LSQ regression algorithm for both aortic layers are listed in table 1.

Downloaded from https://royalsocietypublishing.org/ on 17 November 2021

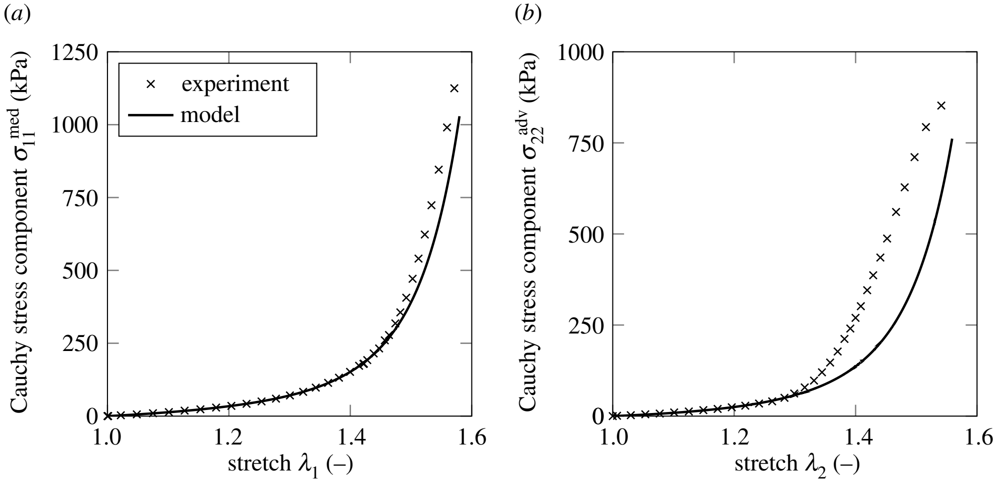

Figure 7. LSQ regression results of the mechanical behaviour of (*a*) the media and (*b*) the adventitia from a dissected human ascending thoracic aorta based on experimental results from our laboratory. Note that the legend in (*a*) also applies to (*b*).

(ii) Active material response

As mentioned above, there is no suitable experimental study on the active behaviour of SMCs in the human aorta in the literature. Therefore, we followed the approach of Haspinger *et al.* [53], who scaled a set of experimental data from a length–tension experiment with a medial tissue of healthy porcine common carotid arteries from Murtada *et al.* [26]. The set of experimental data from Murtada *et al.* [26] provides the nominal stress of the passive behaviour $\breve{P}_{11r}^{\text{pas}}$ and the overall behaviour $\breve{P}_{11r}^{\text{tot}}$ for each circumferential stretch $\breve{\lambda}_{1r}$. It is assumed that the results can be scaled to human tissue with a stretch offset Λ_λ and a stress offset Λ_P.

We followed this approach in a slightly modified way, applying the conversion of a set of porcine data $\{\breve{\lambda}_{1r}, \breve{P}_{11r}\}$ to a set of scaled human data $\{\lambda_{1r}, P_{11r}\}$, i.e.

$$\lambda_1 = (\breve{\lambda}_1)^{\Lambda_\lambda} \quad \text{and} \quad P_{11}^{\text{pas}} = \Lambda_P \breve{P}_{11}^{\text{pas}}. \tag{4.9}$$

The offsets are chosen so that the passive constitutive model for the media with its previously determined parameter set $\{\mu_g^*, k_1^*, k_2^*, c_1^*, c_2^*\}$ predicts the scaled data P_{11r}^{pas}. By applying the LSQ regression and the experimental data for $\breve{\lambda}_{1r}$ and $\breve{P}_{11r}^{\text{pas}}$, the scale parameters are determined to $\Lambda_\lambda = 0.51$ and $\Lambda_P = 2.31$.

It is assumed that all SMCs are activated during the length–tension experiment, i.e. $\phi_{\text{smc}} = 1$. The mechanical parameters of the constitutive model of contractile SMCs are fitted to the total nominal stress component P_{11}^{tot}, which does not depend on the sign of the radial tilt due to the symmetry of the strip and its assumed constitutive behaviour. That is, the two medial strips in figure 8 produce the same Cauchy stress response. The axial stretch λ_2 and the amount of shear γ follow from the state of traction-free radial and axial surfaces. Since the absolute values of the radially tilted SMCs remain constant over the entire media, it is irrelevant whether the total stress response is fitted to the contraction of a single or several alternating lamellar units. Finally, we can apply the LSQ regression for the given set of experimental data $\{\lambda_{1r}, P_{11r}^{\text{tot}}\}$ from length–tension experiments. The relatively low values of $R^2 \sim 77\%$ are caused by the large uncertainty of the experimental data. Note that the initial deformation state $\mathbf{F}_0$ of the SMCs in the medial strip, which is required for the constitutive model, is easy to grasp, as it corresponds to the uniaxial extension test set-up for the passive media.

Figure 9 shows the comparison between experiment and theory for a radial tilt of 20° [2,7,8], as well as the contraction efficiency $\mu_{\text{smc}}\mathcal{O}(I_{0,\text{smc}})$ for different radial tilts. As expected, the

Downloaded from https://royalsocietypublishing.org/ on 17 November 2021

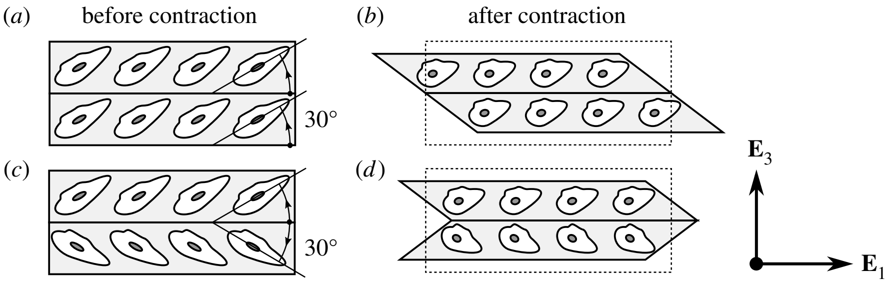

Figure 8. A 2D view of a medial strip consisting of two lamellar units (*a*,*c*) before and (*b*,*d*) after contraction of the SMCs with (*a*,*b*) constant and (*c*,*d*) an alternating radial tilt of 30°.

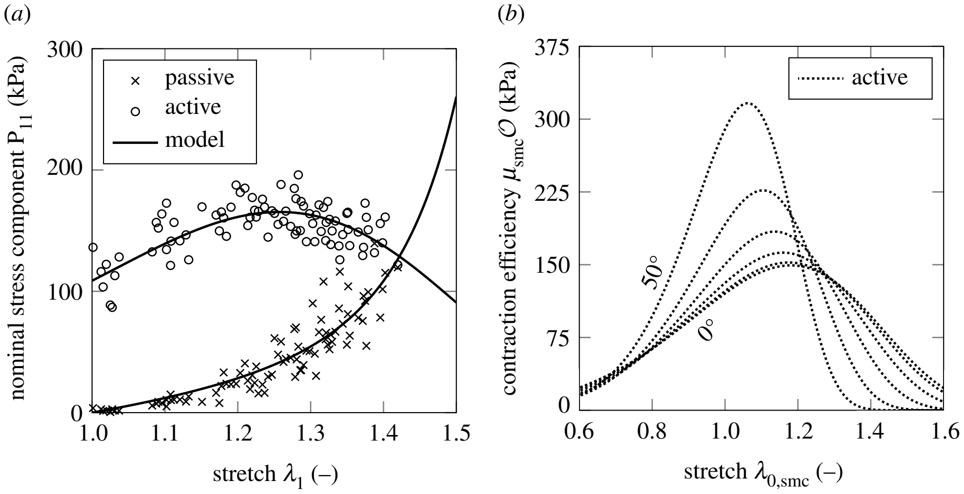

Figure 9. Results of (*a*) the LSQ regression of the length–tension experiments by assuming a radial tilt of 20° and (*b*) the corresponding contraction efficiency of SMCs for different radial tilts, which are based on scaled experimental results from the literature [26]. Note that an increment of 10° was used.

maximum overlap function $\mathcal{O}(I_{\mathrm{opt}} = 1)$ moves to lower initial SMC stretches for large radial tilts. At the same time, the maximum SMC stiffness μ_{smc} increases for larger radial tilts, since a higher stress has to be generated in order to produce the same circumferential stress. Then in figure 10, we demonstrate the induced axial stretch λ_2 and the amount of shear γ of the passive and active material behaviour of the media strip, which is illustrated in figure 8, under an applied uniaxial extension in the circumferential direction. In order to obtain the passive material behaviour, we simply omitted the active contribution of SMCs. The radial tilt has a significant influence on the transverse deformation, as can be seen from the axial stretch λ_2. The medial strip flattens out at larger radial tilts, which seems intuitive as the active SMCs then tend to compress the medial strip. In addition, the amount of shear γ decreases with smaller radial tilts, so that $\gamma = 0$ results for a radial tilt of 0°, which is to be expected owing to the symmetry.

We must emphasize that the approach presented depends on the assumption that the radial tilt in each lamellar unit is constant across the media. A varying radial tilt would lead to an inhomogeneous deformation, which could subsequently lead to a bulging of the specimen. Length–tension experiments should therefore always be carried out in a biaxial test setu-up in order to record as much of the contraction deformation as possible.

Downloaded from https://royalsocietypublishing.org/ on 17 November 2021

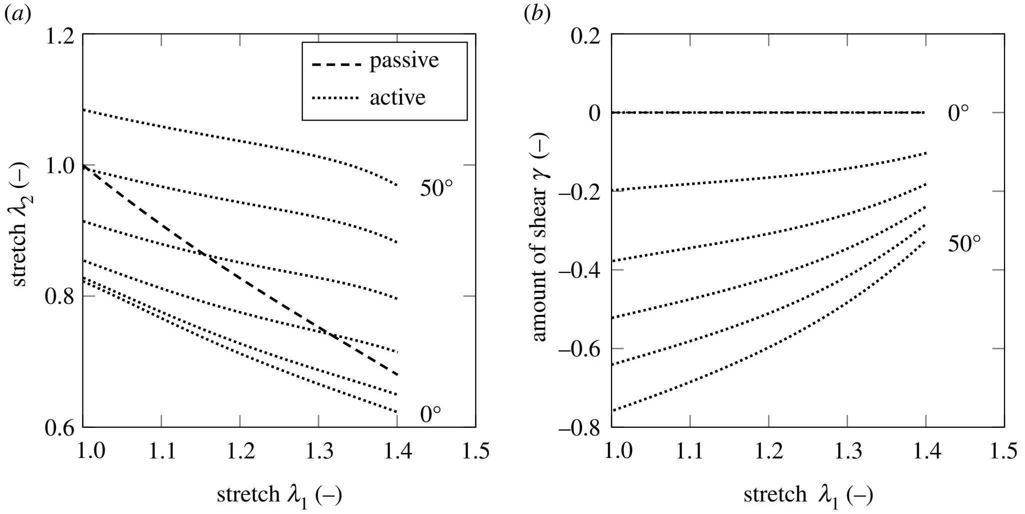

Figure 10. Results of uniaxial extension tests with passive and active material behaviour of the medial strip showing (*a*) the induced axial stretch λ_2 and (*b*) the amount of shear γ over the applied circumferential stretch λ_1 for different radial tilts. Note that the legend in (*a*) also applies to (*b*) and that an increment of 10° was used.

5. Conclusion

We recently proposed to investigate further aspects of the initiation and propagation of aortic dissection by including the active contribution of SMCs in a constitutive model of the human aortic wall [21]. Building on this, we outlined the importance of contractile SMCs in this study and presented a layer-specific constitutive framework that models the passive and active mechanics of the aorta by using a novel, purely mechanical constitutive model of the active contribution of SMCs. We have applied the DFD method, which is based on the original framework proposed by Li *et al.* [16], and modified it to an isoparametric formulation by changing the numerical integration method and implementing a non-uniform discretization of the unit hemisphere in order to efficiently model the dispersed alignment of the fibrous constituents and the dispersed arrangement of SMCs. Experimental data were then collected from our laboratory and from the literature and subsequently used to identify the constitutive parameters. This enabled the initial investigation of the influence of the transmural arrangement of SMCs on the mechanics of a healthy aorta, even without sufficient experimental data. In the present study, however, one can only speculate about a possible transfer of the results obtained to aortic dissection.

The characteristic length–tension behaviour of SMCs is modelled using a Weibull distribution that is suitable to approximate the asymmetric contractile response. The distribution function can be interpreted as the efficiency of actin–myosin motors as a function of their overlap before contraction. The fraction of contractile SMCs reported to change in cardiovascular diseases can be controlled by an independent scalar parameter. The constitutive models of the passive constituents, i.e. ground substance, collagen fibres and elastic fibres, which are required for the formulation of a layer-specific model of the aortic wall, are adapted from previous studies [16,21]. The model for the active stress contribution can be extended in various ways in the light of new experimental data. Contraction-specific parameters such as the stretch with optimal overlap can be made dependent on the position of an SMC in the reference configuration, which enables the introduction of transmural heterogeneity. Another possible extension is the inclusion of tissue remodelling (e.g. [68]), which could alter the contraction behaviour of SMCs by changing their orientation according to an optimality such as the direction of the largest Eulerian principal strain.

Downloaded from https://royalsocietypublishing.org/ on 17 November 2021

In order to evaluate the efficiency of the isoparametric DFD method and the non-uniform discretization of the unit hemisphere, convergence rates were compared for various numerical examples, i.e. uniaxial extension, simple shear and a large-scale computational model. The results suggest that spherical triangles should be chosen in favour of angular elements. In addition, a low-order numerical integration method, such as the centroid rule, provides results that are often even better than results obtained from high-order numerical integration methods. Finally, the large-scale computational model showed that a large number of elementary areas increased the computational time dramatically and, moreover, the results did not improve significantly when the number of elementary areas was increased above 256. However, we emphasize that the discretization of the unit hemisphere has to be chosen depending on the application, since efficiency and accuracy depend heavily on the boundary-value problem and the associated deformation.

The fitting procedure for the various aortic constituents is then detailed. An MLE is used to determine the structural parameters from histological data. Layer-specific PDFs for collagen fibres and partly for SMCs are fitted to statistical data from healthy human thoracic aortic tissue, taken from Holzapfel *et al.* [33] and Schriefl *et al.* [64]; however, there are no quantitative experimental studies on the orientation of elastic fibres nor on the out-of-plane distribution of SMCs in aortas. Therefore certain parameters have to be guessed heuristically. The structural parameters were then determined with experimental data from our laboratory and from the literature [23] in order to determine the remaining mechanical parameters for the passive constituents. Then, we applied the LSQ regression to obtain the mechanical parameters of passive and active mechanics of the aorta.

To determine the passive parameters, layer-specific uniaxial extension tests were used from dissected thoracic human aortas, which come from our laboratory. However, the regression results showed that a non-physical exponential stiffening occurs at higher stretches, which is a limitation of the exponential model used. Since high stretches are known to be non-physiological, the model is therefore not used within this domain. However, by increasing the number of parameters used for the LSQ regression, the results of the model regression could be improved. This would cause the parameters to lose their physical meaning. In addition, unsuitable parameter ratios can be obtained, which lead to undesirable material behaviour, such as an auxetic behaviour [69]. Therefore, we wanted to provide a set of parameters in this study, all of which have a physical meaning. In other words, every single parameter should be based on experimental results. Under this condition, we had to use experimental data from different sources, which subsequently affects the quality of the result. Other models, such as bilinear models [69,70], could be considered as replacements, but it is questionable whether similar results could be delivered.

For the active parameters, because of the lack of experimental work on the characteristic length–tension behaviour of human vascular SMCs, the experimental results of Murtada *et al.* [26] on healthy porcine thoracic aortic tissue were scaled to human proportions, which corresponds to an approach proposed by Haspinger *et al.* [53]. In addition, the constitutive model for active SMCs is fitted for different radial tilts, which has a significant influence on the deformation after contraction of the tissue.

One limitation of this study is that the experimental data used for the fitting process originate from different donors, in different locations and with unequal health situations. This is due to the limited availability of experimental data. To the best of the authors' knowledge, there is no study documented in the literature in which structural investigations and mechanical tests, both passive and active, were performed on a single healthy or diseased donor. Therefore, we collected experimental data from various studies in order to obtain realistic fitting results in the setting of dissected human tissue. Within the context of this study, only initial computational results on the influence of the radial tilt of contractile SMCs could be shown.

In summary, we derive the following conclusions from this study. First, the DFD method can also be used in connection with dispersed SMCs. In addition, a low-order numerical integration method is often sufficient and a non-uniform discretization over the unit hemisphere is of only limited use to the computational results, as it depends on the application and the associated local

Downloaded from https://royalsocietypublishing.org/ on 17 November 2021

deformation. However, when used appropriately, this can significantly increase computational efficiency. In addition, even a small number of elementary areas can express the results of a large-scale computational model with only a few deviations. Second, in the absence of sufficient experimental data, the results indicate that the active contribution of SMCs has a remarkable impact on the mechanics of the healthy aorta. As mentioned above, it is crucial that the constitutive model for SMC activity be fitted to representative experimental data. In particular, a biaxial test set-up for length–tension experiments on human tissue and histological investigations of the SMC arrangement are prerequisites for carrying out realistic simulations. In the present case, the multiaxial nature of the deformation after contraction leads to large uncertainties in the regression to uniaxial extension data. Third, the radial tilt has a noticeable influence on the mechanical behaviour of the aorta. Since the vessel wall follows the principle of optimal operation, which tries to maintain a preferred state of mechanical stress [71], it can be assumed that the aorta is able to produce a wide range of transmural stress gradients by varying the arrangement of SMCs. Even if the induced shear deformation is comparatively small, its influence should not be underestimated, since additional normal stresses are generated in finite elasticity [18]. In addition, if a shear deformation occurs in sensitive areas of the aortic wall and exceeds a critical threshold, the elastic lamellae can tear from the SMCs. An aortic dissection can then be initiated from these sites [11].

To conclude, it can be said that the proposed purely mechanical constitutive law for the active contribution of SMCs is straightforward to use and implement, but also general enough to reflect the characteristic length–tension behaviour of SMCs of the aorta. The fitting procedure provides an insight into available experimental data and open questions. In the future, this method will also be suitable for application to novel experimental data. Moreover, the proposed constitutive model will be applied to selected applications in a follow-up study in order to investigate the influence of the radial tilt of contractile SMCs in both healthy and diseased aortas. Its simplicity in combination with an efficient and isoparametric DFD method will enable future use in large-scale computational models.

Data accessibility. Source codes for Python (§3) and for Matlab [60] (§4) are available from: https://repository.tugraz.at/records/bvz3x-1wk71.

Authors' contributions. M.R.-P. conceived and designed the study, carried out the design of the figures and drafted the manuscript; M.R.-P., M.P.W and D.R.Q.P. performed the numerical analysis and analytical studies of the models; M.P.W. and D.R.Q.P. participated in the design of the study and drafted the manuscript; G.A.H. helped to conceptualize and design the study, coordinated the study and critically revised the manuscript. All authors have given their final approval to the publication and agree to be responsible for the work carried out therein.

Competing interests. We declare we have no competing interests.

Funding. The work was supported by the Lead Project on 'Mechanics, Modeling and Simulation of Aortic Dissection', granted by Graz University of Technology, Graz, Austria.

Acknowledgements. We thank Selda Sherifova (Graz University of Technology, Institute of Biomechanics) for providing uniaxial extension test results of a dissected human thoracic aorta.

References

1. Shen Y, LeMaire S. 2017 Molecular pathogenesis of genetic and sporadic aortic aneurysms and dissections. *Curr. Probl. Surg.* **54**, 95–155. (doi:10.1067/j.cpsurg.2017.01.001)
2. Dingemans KP, Teeling P, Lagendijk JH, Becker AE. 2000 Extracellular matrix of the human aortic media: an ultrastructural histochemical and immunohistochemical study of the adult aortic media. *Anat. Rec.* **258**, 1–14. (doi:10.1002/(ISSN)1097-0185)
3. Murtada SI, Kroon M, Holzapfel GA. 2010 Modeling the dispersion effects of contractile fibers in smooth muscles. *J. Mech. Phys. Solids* **58**, 2065–2082. (doi:10.1016/j.jmps.2010.09.003)
4. Guilford WH, Warshaw DM. 1998 The molecular mechanics of smooth muscle myosin. *Comp. Biochem. Physiol. B* **119**, 451–458. (doi:10.1016/S0305-0491(98)00002-9)
5. Lowy J, Small JV. 1970 The organization of myosin and actin in vertebrate smooth muscle. *Nature* **227**, 46–51. (doi:10.1038/227046a0)

Downloaded from https://royalsocietypublishing.org/ on 17 November 2021

6. Walmsley JG, Canham PB. 1979 Orientation of nuclei as indicators of smooth muscle cell alignment in the cerebral artery. *Blood Vessels* **16**, 43–51. (doi:10.1159/000158189)
7. O'Connell MK *et al.* 2007 The three-dimensional micro- and nanostructure of the aortic medial lamellar unit measured using 3D confocal and electron microscopy imaging. *Matrix Biol.* **27**, 171–181. (doi:10.1016/j.matbio.2007.10.008)
8. Fujiwara T, Uehara Y. 1992 The cytoarchitecture of the medial layer in rat thoracic aorta: a scanning electron-microscopic study. *Cell Tissue Res.* **270**, 165–172. (doi:10.1007/BF00381891)
9. Rhodin JAG. 1980 Architecture of the vessel wall. In *Handbook of physiology, the cardiovascular system* (eds DF Bohr, AD Somlyo, HV Sparks), vol. 2, pp. 1–31. Bethesda, MD: American Physiologial Society.
10. Halushka MK *et al.* 2016 Consensus statement on surgical pathology of the aorta from the Society for Cardiovascular Pathology and the Association for European Cardiovascular Pathology: II. Noninflammatory degenerative diseases—nomenclature and diagnostic criteria. *Cardiovasc. Pathol.* **25**, 247–257. (doi:10.1016/j.carpath.2016.03.002)
11. Sugita S, Kato M, Wataru F, Nakamura M. 2020 Three-dimensional analysis of the thoracic aorta microscopic deformation during intraluminal pressurization. *Biomech. Model. Mechanobiol.* **19**, 147–157. (doi:10.1007/s10237-019-01201-w)
12. Humphrey JD. 2013 Possible mechanical roles of glycosaminoglycans in thoracic aortic dissection and associations with dysregulated transforming growth factor-β. *J. Vasc. Res.* **50**, 1–10. (doi:10.1159/000342436)
13. Erdheim J. 1929 Medionecrosis aortae idiopathica. *Virch. Arch. Pathol. Anat.* **273**, 454–479. (doi:10.1007/BF02158989)
14. Nakashima Y. 2001 Pathophysiology of aortic dissection and abdominal aortic aneurysm. In *Cardio-aortic and aortic surgery* (eds S Kawada, T Ueda, H Shimizu), pp. 4–11. Tokyo, Japan: Springer.
15. Lee JH, Kim J, Lee SJ, Kim YA, Maeng YI, Park KK. 2020 Apoptosis and fibrosis of vascular smooth muscle cells in aortic dissection: an immunohistochemical study. *Int. J. Clin. Exp. Pathol.* **13**, 1962–1969.
16. Li K, Ogden RW, Holzapfel GA. 2018 A discrete fibre dispersion method for excluding fibres under compression in the modelling of fibrous tissues. *J. R. Soc. Interface* **15**, 20170766. (doi:10.1098/rsif.2017.0766)
17. Holzapfel GA, Ogden RW, Sherifova S. 2019 On fibre dispersion modelling of soft biological tissues: a review. *Proc. Math. Phys. Eng. Sci.* **475**, 20180736. (doi:10.1098/rspa.2018.0736)
18. Holzapfel GA. 2000 *Nonlinear solid mechanics. A continuum approach for engineering*. Chichester, UK: John Wiley & Sons.
19. Holzapfel GA, Gasser TC, Ogden RW. 2000 A new constitutive framework for arterial wall mechanics and a comparative study of material models. *J. Elast.* **61**, 1–48. (doi:10.1023/A:1010835316564)
20. Holzapfel GA, Niestrawska JA, Ogden RW, Reinisch AR, Schriefl AJ. 2015 Modelling non-symmetric collagen fibre dispersion in arterial walls. *J. R. Soc. Interface* **12**, 1–14. (doi:10.1098/rsif.2015.0188)
21. Rolf-Pissarczyk M, Li K, Fleischmann D, Holzapfel GA. 2021 A discrete approach for modeling degraded elastic fibers in aortic dissection. *Comput. Methods Appl. Mech. Eng.* **373**, 113511. (doi:10.1016/j.cma.2020.113511)
22. Markert B, Ehlers W, Karajan N. 2005 A general polyconvex strain-energy function for fiber-reinforced materials. *Proc. Appl. Math. Mech.* **5**, 245–246. (doi:10.1002/pamm.200510099)
23. Matsumoto T, Sugita S, Nagayama K. 2016 Tensile properties of smooth muscle cells, elastin, and collagen fibers. In *Vascular engineering* (eds K Tanishita, K Yamamoto), pp. 127–140. Tokyo, Japan: Springer.
24. Ogden RW. 2016 Nonlinear continuum mechanics and modelling the elasticity of soft biological tissues with a focus on artery walls. In *Lecture notes from the summer school 'Biomechanics: trends in modeling and simulation' in Graz, Austria, in September, 2014* (eds GA Holzapfel, RW Ogden), pp. 83–156. Berlin, Germany: Springer.
25. Hai CM, Murphy RA. 1988 Cross-bridge phosphorylation and regulation of latch state in smooth muscle. *Am. J. Physiol.-Cell Physiol.* **254**, C99–C106. (doi:10.1152/ajpcell.1988.254.1.C99)
26. Murtada SI, Arner A, Holzapfel GA. 2012 Experiments and mechanochemical modeling of smooth muscle contraction: significance of filament overlap. *J. Theor. Biol.* **297**, 176–186. (doi:10.1016/j.jtbi.2011.11.012)

Downloaded from https://royalsocietypublishing.org/ on 17 November 2021

27. Murtada SI, Lewin S, Arner A, Holzapfel GA. 2016 Adaptation of active tone in the mouse descending thoracic aorta under acute changes in loading. *Biomech. Model. Mechanobiol.* **15**, 579–592. (doi:10.1007/s10237-015-0711-z)
28. Murtada SI, Humphrey JD, Holzapfel GA. 2017 Multiscale and multiaxial mechanics of vascular smooth muscle. *Biophys. J.* **113**, 714–727. (doi:10.1016/j.bpj.2017.06.017)
29. Stålhand J, Klarbring A, Holzapfel GA. 2011 A mechanochemical 3D continuum model for smooth muscle contraction under finite strains. *J. Theor. Biol.* **268**, 120–130. (doi:10.1016/j.jtbi.2010.10.008)
30. Stålhand J, McMeeking RM, Holzapfel GA. 2016 On the thermodynamics of smooth muscle contraction. *J. Mech. Phys. Solids* **94**, 490–503. (doi:10.1016/j.jmps.2016.05.018)
31. Fung YC. 1997 *Biomechanics: circulation*, 2nd edn. Berlin, Germany: Springer.
32. Walmsley JG, Murphy RA. 1987 Force–length dependence of arterial lamellar, smooth muscle, and myofilaments orientations. *Am. J. Physiol.-Heart Circ. Physiol.* **253**, 1141–1147. (doi:10.1152/ajpheart.1987.253.5.H1141)
33. Holzapfel GA, Gasser TC, Stadler M. 2002 A structural model for the viscoelastic behavior of arterial walls continuum formulation and finite element analysis. *Eur. J. Mech. A-Solids* **21**, 441–463. (doi:10.1016/S0997-7538(01)01206-2)
34. Lundholm L, Mohme-Lundholm E. 1966 Length at inactivated contractile elements, length–tension diagram, active state and tone of vascular smooth muscle. *Acta Physiol. Scand.* **68**, 347–359. (doi:10.1111/apha.1966.68.issue-3-4)
35. Herlihy JT, Murphy RA. 1973 Length–tension relationship of smooth muscle of the hog carotid artery. *Circ. Res.* **33**, 275–283. (doi:10.1161/01.RES.33.3.275)
36. Huo Y, Cheng Y, Zhao X, Lu X, Kassab GS. 2012 Biaxial vasoactivity of porcine coronary artery. *Am. J. Physiol.-Heart Circ. Physiol.* **302**, H2058–H2063. (doi:10.1152/ajpheart.00758.2011)
37. Cox RH. 1975 Arterial wall mechanics and composition and the effects of smooth muscle activation. *Am. J. Physiol.* **229**, 807–812. (doi:10.1152/ajplegacy.1975.229.3.807)
38. Cox RH. 1978 Regional variation of series elasticity in canine arterial smooth muscles. *Am. J. Physiol.-Heart Circ. Physiol.* **234**, H542–H551. (doi:10.1152/ajpheart.1978.234.5.H542)
39. Dobrin PB, Rovick AA. 1969 Influence of vascular smooth muscle on contractile mechanics and elasticity of arteries. *Am. J. Physiol.* **217**, 1644–1651. (doi:10.1152/ajplegacy.1969.217.6.1644)
40. Dobrin PB. 1973 Influence of initial length on length–tension relationship of vascular smooth muscle. *Am. J. Physiol.* **225**, 664–670. (doi:10.1152/ajplegacy.1973.225.3.664)
41. Gordon AR, Siegman MJ. 1971 Mechanical properties of smooth muscle. I. Length–tension and force–velocity relations. *Am. J. Physiol.* **221**, 1243–1249. (doi:10.1152/ajplegacy.1971.221.5.1243)
42. Siegman MJ, Davidheiser S, Mooers SU, Butler TM. 2013 Structural limits on force production and shortening of smooth muscle. *J. Muscle Res. Cell Motil.* **34**, 34–60. (doi:10.1007/s10974-012-9333-6)
43. Gill RC, Cote KR, Bowes KL, Kingma YJ. 1986 Human colonic smooth muscle spontaneous contractile activity and response to stretch. *Gut* **27**, 1006–1013. (doi:10.1136/gut.27.9.1006)
44. Chin LYM, Bossé Y, Hackett TL, Paré PD, Seow CY. 2010 Human airway smooth muscle is structurally and mechanically similar to that of other species. *Eur. Respir. J.* **36**, 170–177. (doi:10.1183/09031936.00136709)
45. de Beaufort HWL, Ferrara A, Conti M, Moll FL, van Herwaarden JA, Figueroa CA, Bismuth J, Auricchio F, Trimarchi S. 2018 Comparative analysis of porcine and human thoracic aortic stiffness. *Eur. J. Vasc. Endovasc.* **55**, 560–566. (doi:10.1016/j.ejvs.2017.12.014)
46. Wang L, Paré PD, Seow CY. 2001 Selected contribution: effect of chronic passive length change on airway smooth muscle length–tension relationship. *J. Appl. Physiol.* **90**, 734–740. (doi:10.1152/jappl.2001.90.2.734)
47. Rachev A, Hayashi K. 1999 Theoretical study of the effects of vascular smooth muscle contraction on strain and stress distributions in arteries. *Ann. Biomed. Eng.* **27**, 459–468. (doi:10.1114/1.191)
48. Gleason RL, Taber LA, Humphrey JD. 2004 A 2-D model of flow-induced alterations in the geometry, structure, and properties of carotid arteries. *J. Biomed. Eng.* **126**, 371–381. (doi:10.1115/1.1762899)
49. Horvat N, Virag L, Holzapfel GA, Sorić J, Karšaj I. 2019 A finite element implementation of a growth and remodeling model for soft biological tissues: verification and

Downloaded from https://royalsocietypublishing.org/ on 17 November 2021

application to abdominal aortic aneurysms. *Comput. Method Appl. Mech. Eng.* **352**, 586–605. (doi:10.1016/j.cma.2019.04.041)

50. VanBavel E, Mulvany MJ. 1994 Role of wall tension in the vasoconstrictor response of cannulated rat mesenteric small arteries. *J. Physiol.* **477**, 103–115. (doi:10.1113/jphysiol.1994.sp020175)
51. Carlson BE, Secomb TW. 2005 A theoretical model for the myogenic response based on the length–tension characteristics of vascular smooth muscle. *Microcirculation* **12**, 327–338. (doi:10.1080/10739680590934745)
52. Chen H, Luo T, Zhao X, Huo Y, Kassab GS. 2013 Microstructural constitutive model of active coronary media. *Biomaterials* **34**, 7575–7583. (doi:10.1016/j.biomaterials.2013.06.035)
53. Haspinger DC, Murtada SI, Niewstrawska JA, Holzapfel GA. 2018 Numerical analyses of the interrelation between extracellular smooth muscle orientation and intracellular filament overlap in the human abdominal aorta. *Z. Angew. Math. Mech.* **98**, 2198–2221. (doi:10.1002/zamm.v98.12)
54. Costabal FS, Choy JS, Sack KL, Guccione JM, Kassab GS, Kuhl E. 2019 Multiscale characterization of heart failure. *Acta Biomater.* **86**, 66–76. (doi:10.1016/j.actbio.2018.12.053)
55. Burkardt J. 2010 Estimate integrals over spherical triangles. See people.sc.fsu.edu/~jburkardt/f_src/sphere_triangle_quad/sphere_triangle_quad.
56. Atkinson K. 1982 Numerical integration on the sphere. *J. Aust. Math. Soc. B* **23**, 332–347. (doi:10.1017/S0334270000000278)
57. Boal N, Domínguez V, Sayas FJ. 2008 Asymptotic properties of some triangulations of the sphere. *J. Comput. Appl. Math.* **211**, 11–22. (doi:10.1016/j.cam.2006.11.012)
58. Zwillinger D. 1995 *CRC standard mathematical tables and formulae*, 33rd edn. Boca Raton, FL: CRC Press.
59. Hesse K, Sloan IH, Womersley RS. 2015 Numerical integration on the sphere. In *Handbook of geomathematics*, pp. 2671–2710. Berlin, Germany: Springer.
60. The MathWorks Inc. 2018 *MATLAB*. Natick, MA: The Mathworks Inc.
61. Taylor RL. 2017 *FEAP—a finite element analysis program, version 8.5 user manual*. Berkeley, CA: University of California at Berkeley.
62. Wolfram Research, Inc. 2016 *Mathematica, version 11.0*. Champaign, IL: Wolfram Research, Inc.
63. Dassault Systèmes Simulia Corporation. 2017 *ABAQUS/standard user's manual, version 2017*. Johnston, RI: Dassault Systèmes Simulia Corporation.
64. Schriefl AJ, Zeindlinger G, Holzapfel GA. 2012 Determination of the layer-specific distributed collagen fibre orientations in human thoracic and abdominal aortas and common iliac arteries. *J. R. Soc. Interface* **9**, 1275–1286. (doi:10.1098/rsif.2011.0727)
65. Lillie MA, Shadwick JM, Gosline JM. 2010 Mechanical anisotropy of inflated elastic tissue from the pig aorta. *J. Biomech.* **43**, 2070–2078. (doi:10.1016/j.jbiomech.2010.04.014)
66. Tonar Z, Kochova P, Cimrman R, Perktold J, Witter K. 2015 Segmental differences in the orientation of smooth muscle cells in the tunica media of porcine aortae. *Biomech. Model. Mechanobiol.* **14**, 315–332. (doi:10.1007/s10237-014-0605-5)
67. Weisbecker H, Viertler C, Pierce DM, Holzapfel GA. 2013 The role of elastin and collagen in the softening behavior of the human thoracic aortic media. *J. Biomech.* **46**, 1859–1865. (doi:10.1016/j.jbiomech.2013.04.025)
68. Vigliotti A, Ronan W, Baaijens FPT, Deshpande VS. 2016 A thermodynamically motivated model for stress-fiber reorganization. *Biomech. Model. Mechanobiol.* **15**, 761–789. (doi:10.1007/s10237-015-0722-9)
69. Fereidoonnezhad B, O'Connor C, McGarry JP. 2020 A new anisotropic soft tissue model for elimination of unphysical auxetic behaviour. *J. Biomech.* **111**, 110006. (doi:10.1016/j.jbiomech.2020.110006)
70. Zhang W, Kassab GS. 2007 A bilinear stress-strain relationship for arteries. *Biomaterials* **28**, 1307–1315. (doi:10.1016/j.biomaterials.2006.10.022)
71. Humphrey JD, Schwartz MA, Tellides G, Milewicz DM. 2015 Role of mechanotransduction in vascular biology focus on thoracic aortic aneurysms and dissections. *Circ. Res.* **116**, 1448–1461. (doi:10.1161/CIRCRESAHA.114.304936)